Performance Benefits of Multiwall Carbon Nanotubes in the Polymer Electrolyte Membrane Fuel Cell Gas Diffusion Layer

J. Lee, R. Banerjee, N. Ge, S. Chevalier, M. G. George, H. Liu, P. Shrestha, D. Muirhead, J. Hinebaugh, and A. Bazylak

Thermofluids for Energy and Advanced Material Laboratory
Department of Mechanical and Industrial Engineering,
Institute for Sustainable Energy,
Faculty of Applied Science and Engineering, University of Toronto,
Toronto, Ontario, M5S 3G8, Canada

A commercial gas diffusion layer (GDL) with a microporous layer (MPL) containing multiwall carbon nanotubes (MWCNT) exhibited better performance in a polymer electrolyte membrane (PEM) fuel cell than that with a conventional GDL. This performance benefit was attributed to improved oxygen mass transport in the cathode GDL. The operation of the fuel cell was visualized with synchrotron X-ray radiography to measure the liquid water saturation in the two GDLs. A higher liquid water saturation was measured in the operating fuel with the MWCNT-based MPL than with the conventional MPL. But, the MWCNTs induced higher effective porosity within the GDL, allowing for improved overall oxygen transport, and thus the cell performed better even with higher saturation of liquid water in the GDL.

Introduction

One of the key challenges in the operation of PEM fuel cell stems from product liquid water in the cathode catalyst layer (CL). If excessive liquid water accumulates in the gas diffusion layer (GDL), it inhibits the mass transport of oxygen in the fuel cell. Oxygen diffusion in a liquid-water-saturated GDL is reduced, and this leads to the potential loss and unstable performance of the cell (1,2). For improved liquid water management, a dual-layer GDL containing a carbon fiber substrate and a microporous layer (MPL) has been adopted (3-7).

The MPL is typically comprised of carbon black particles and a hydrophobic agent. Recent findings (8-16) suggested that nano-carbon additive materials in the MPL can further enhance the performance of the fuel cell. Park et al. (8) showed that the adoption of carbon nanofibers and carbon nanotubes (CNT) in the MPL resulted in improved air permeability and reduced thickness. Similarly, Gharibi et al. (9) indicated that the addition of multiwall carbon nanotubes (MWCNT) to the MPL increased gas permeability, pore volume, and electrical conductance. Kannan et al. (10,11) demonstrated that MPLs containing nano-fibrous carbon and PUREBLACK® (Superior Graphite Co., Chicago, IL) improved the power output of the fuel cell. Scheweiss et al. (12,13) reported that an MWCNT-doped MPL (SGL 25 BN) exhibited better transport and electrical properties than the reference GDL (SGL 25 BC). The combination of carbon black and MWCNTs

resulted in a high porosity MPL with hydrophilic pathways for liquid water, and these pathways contributed to the effective removal of liquid water in the cathode. To provide detailed insight into mass transport properties of the MWCNT-based MPL affecting the performance of the fuel cell, it is necessary to quantity liquid water saturation in the GDLs of an operating fuel cell.

Synchrotron X-ray imaging is a unique method that is capable of resolving the liquid water accumulation in the GDL at micron-scale (17,18). Haußmann et al. (19,20) visualized water evolving in the cracks and perforated holes in the GDL suggesting that these were the preferential locations for water accumulation. Lee et al. (21) investigated the impact of the thickness of the MPL in the water distribution in the GDL, and concluded that thinner MPLs resulted in less water content. Zenyuk et al. (22) identified liquid water content in the GDL at varying compressions, and showed that injected water established pathways in the part of the GDL under the channel at high compression. However, synchrotron X-ray imaging has not been widely employed in studying novel GDLs such as the one with a MWCNTs-based MPL.

In this work, fuel cells with commercial GDLs with and without MWCNTs were compared. The through-plane porosity distribution of GDLs were obtained by segmenting 3D computed tomographic images. The fuel cell was also operated at a synchrotron facility to visualize the liquid water evolution and accumulation through 2-D radiography. Combining porosity distributions and in-operando 2D water thickness profiles obtained by synchrotron imaging yielded water saturation profiles in both GDLs. We examined the relationship between mass transport losses in the fuel cell performance and effective porosity of the cathode GDL accounting for water saturation.

Experimental

Fuel Cell Component and Operation

Gas Diffusion Layers. Two commercially available GDLs of the SGL® 25 series (Sigarcet Group, Germany) were studied: 25 BC and 25 BN. Manufacturer specifications of these GDLs are provided in Table 1. Both GDLs have the same fiber substrate structure with 5 wt. % polytetrafluoroethylene (PTFE) treatment. SGL 25 BC has an MPL composed of 23 wt. % PTFE and acetylene black. The MPL of SGL 25 BN consisted of 15 wt. % PTFE, 21 wt. % MWCNTs and acetylene black (12,13). The compressed thickness of the GDL in the fuel cell assembly was controlled by placing 188-μm-thick polyethylene naphthalate (PEN) film spacers around the active area with a 15-μm-thick CL. The resulting compressed thickness of the GDLs in assembled fuel cells are also reported in Table 1.

Operation of Fuel Cells. A fuel cell with an active area of 0.85×0.80 cm^2 was utilized for performing visualization as in our previous works (23-25). Nafion HP (DuPont), a thin and reinforced membrane, was chosen for reduced swelling effects during the operation of the fuel cell. The membrane was coated with a catalyst with a platinum loading of 0.3 mg/cm^2 (both anode and cathode) (Ion Power, NC). The bipolar plate (BPP) was engraved with identical parallel 0.5 mm channels and lands in the direction of the X-ray beam.

TABLE I. Manufacturer specifications of SGL GDLs (25 BC and 25 BN) and the assembly compression ratios. *Manufacturer specifications.

Properties	Unit	25 BC	25 BN
Areal Weight*	g/m²	90 ± 10	65
Thickness @ 5PSI*		235 ± 20	228
Thickness @ 1MPa*	μm	190 ± 20	165
Thickness @ 2MPa*		170 ± 20	-
TP Electric Resistance @ 1MPa*	mOhm x cm²	< 12	5.3
IP Pressure Drop @ 1MPa*	mbar	< 1100	645
PTFE treatment on the substrate*	wt. %	5	5
MPL composition*	-	23 wt. % PTFE	15 wt. % PTFE 21wt. %CNTs
Assembly compression ratio	%	26.4	24.1

The fuel cells were controlled with an 850e Scribner Fuel Cell Testing System (Scribner Associates Inc., NC). The temperature of the fuel cell was maintained at 60°C with an external water circulation bath, while pure hydrogen and air at 1 slpm were supplied to the anode and cathode, respectively. Both reactant gases were fully humidified at a dew point of 60°C (100% relative humidity), and back-pressurized to 200 kPa (absolute). The current density was increased from 0 A/cm^2 with an increment of 0.5 A/cm^2 until the limiting current was reached. Each current density was held constant for 15 minutes in order to ensure stable performance and steady state liquid water content.

Measurement of Liquid Water Saturation

Through-plane Porosity Profiles of GDLs. A desktop Skyscan 1172 (Bruker, Billerica, MA) micro-computed tomography device was utilized to acquire 3-dimensional images of the GDL at a pixel size of 3.14 μm with the energy level of 36 keV. Raw images were reconstructed using NRecon software (Bruker, Billerica, MA). Each in-plane image was segmented by an in-house procedure (26-30). The number of in-plane slices was equivalent to the thickness of the GDL from the CL to bi-polar plate (y-direction). Grey scale pixels in the images were segmented into three phases, which were void space, carbon fiber in the substrate and MPL, and a through-plane porosity profile of the GDL was obtained. For detailed description of the segmentation algorithm and the procedure for obtaining the through-plane porosity distribution of the GDL, readers are referred to (29,31).

In-situ Measurement of Liquid Water Thickness with Synchrotron X-ray. Radiographs of operating fuel cells were taken at the Biomedical Imaging Therapy Bending Magnet (05B1-1) beamline in the Canadian Light Source (Saskatoon, Canada) (32). The images were acquired at an energy level of 24 keV, with a pixel resolution of 6.5 μm and a temporal resolution of 3 seconds per frame. In Figure 1, a schematic of the X-ray radiography imaging of the fuel cell at the synchrotron beamline is illustrated. To quantify liquid water, raw images were processed by in-house developed algorithm based on Beer-Lambert law (23-25):

$$I_{wet} = I_{dry} \times e^{-\mu x} \qquad [1]$$

where I_{wet} is the pixel intensity of frames during operation, I_{dry} is the pixel intensity of frames at open circuit voltage (OCV), μ is the X-ray attenuation coefficient of liquid water in cm^{-1} at 24 KeV, and x represents the thickness of liquid water [cm]. The X-ray attenuation coefficient of liquid water was measured with an ex-situ device that held known quantities of liquid water (23). The water thickness in the cathode GDL measured in the processed synchrotron imaging was combined with the porosity of the GDL to calculate the saturation level of GDL. The saturation, which represents the fraction of pore space occupied by liquid water, was obtained as following:

$$s(y) = \frac{x(y)}{\varepsilon(y) \times 0.80} \qquad [2]$$

where $s(y)$ represents the saturation at the through-plane position y, $x(y)$ is the thickness of liquid water at y in cm, $\varepsilon(y)$ is the porosity at y, and 0.80 is length of the active area in the path of the beam, in cm.

For further analysis, the effective porosity, the fraction of pores unoccupied by liquid water that is available for oxygen transport, was calculated as follows:

$$\varepsilon(y)_{eff} = \varepsilon(y)(1 - s(y)) \qquad [3]$$

where $\varepsilon(y)_{eff}$ is the effective porosity at the through-plane position y, $\varepsilon(y)$ and $s(y)$ are the porosity and saturation at y, respectively.

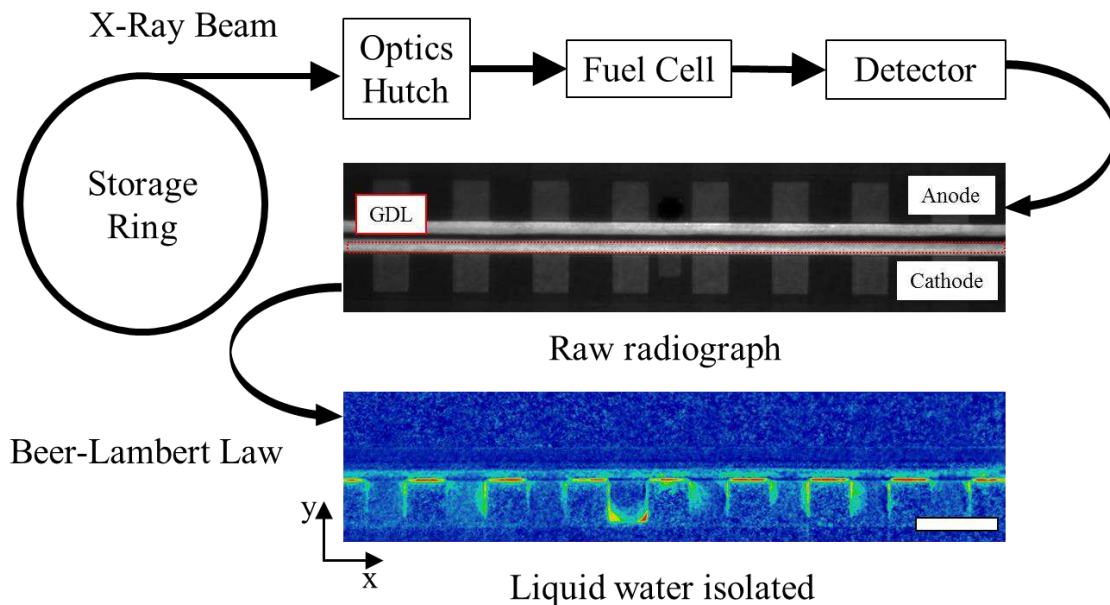Figure 1. A schematic of in situ visualization of liquid water in an operating fuel cell at the synchrotron facility. The scale bar indicates 1 mm.

Results and Discussion

Electrochemical Behaviors of Fuel Cells

The IR-compensated polarization curves of fuel cells with SGL 25 BC and BN are shown in Figure 2. High frequency resistances (electrical resistances) were measured at each current density, which are presented on the right Y-axis of Figure 2. SGL 25 BN exhibited superior performance to SGL 25 BC. At current densities of 2000 mA/cm^2, the fuel cell with SGL 25 BC exhibited potential degradation due to limited oxygen transport in the cathode GDL, which became more severe at 2500 mA/cm^2. The fuel cell with SGL 25 BN did not show significant mass transport losses throughout all operating current densities.
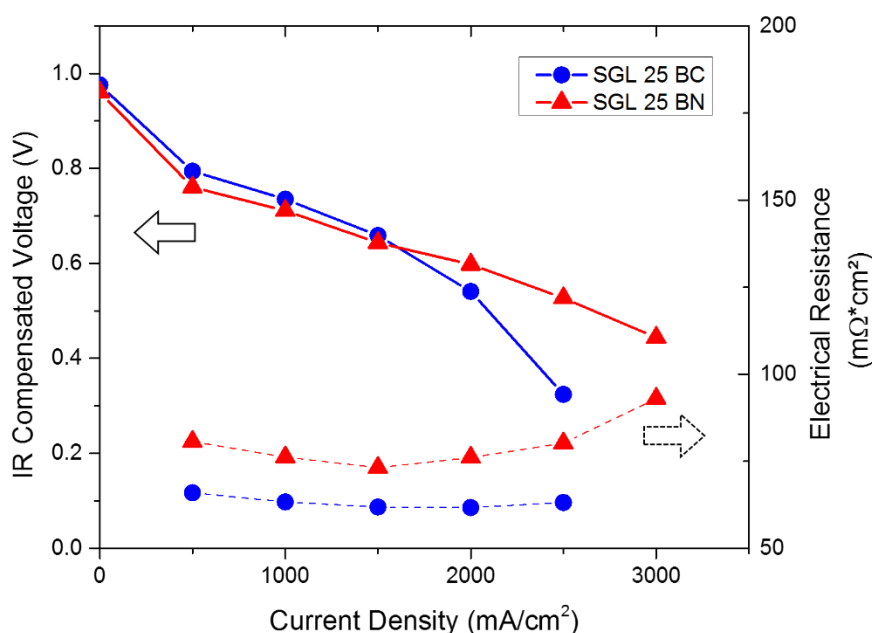
Figure 2. IR-compensated polarization curves (left Y-axis) and electrical resistances (right Y-axis) of fuel cells with SGL 25 BC and BN. The fuel cell was operated at 60°C. Both reactant gases were fully humidified at a dew point of 60°C (100% relative humidity), and back-pressurized to 200 kPa (absolute).

Liquid Water Saturation in the Cathode GDL

Liquid water saturation in SGL 25 BC and BN at 1.0, 1.5, 2.0 and 2.5 A/cm^2 operations are presented in Figure 3. At through-plane positions between 20-60 μm, liquid water saturation in SGL 25 BN was significantly higher than BC. As reported by Schweiss et al. (12,13), the addition of MWCNTs not only affects porosity and pore size distribution within the MPL, but also influences MPL-substrate interaction. We confirmed using our segmented CT images that SGL 25 BN exhibited a lower content of MPL particles impregnated in the substrate, which left larger pores in the MPL-substrate region that were susceptible to liquid water accumulation.
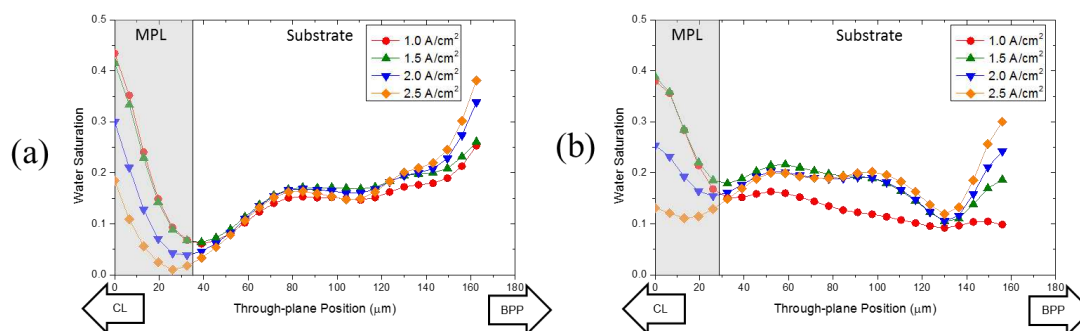
Figure 3. Liquid water saturation profiles in SGL 25 (a) BC and (b) BN at 1.0, 1.5, 2.0 and 2.5 A/cm^2. The left of the profile indicates the CL, and the right indicates bipolar-plate (BPP). The thickness of the bulk MPL (shaded region) is equivalent to the thickness difference between SGL 25 BC/BN and the substrate (SGL 25 BA).

To further understand oxygen transport in the saturated GDLs in the operating fuel cell, effective porosities in SGL 25 BC and BN were obtained as illustrated in Figure 4. Effective pores are pores that are not invaded by liquid water and are available for oxygen transport. Figure 4 depicts that the fraction of effective pores was less in SGL 25 BC than 25 BN despite the lower water saturation. This was due to the high solid fraction that includes MPL and carbon fiber material in SGL 25 BC.
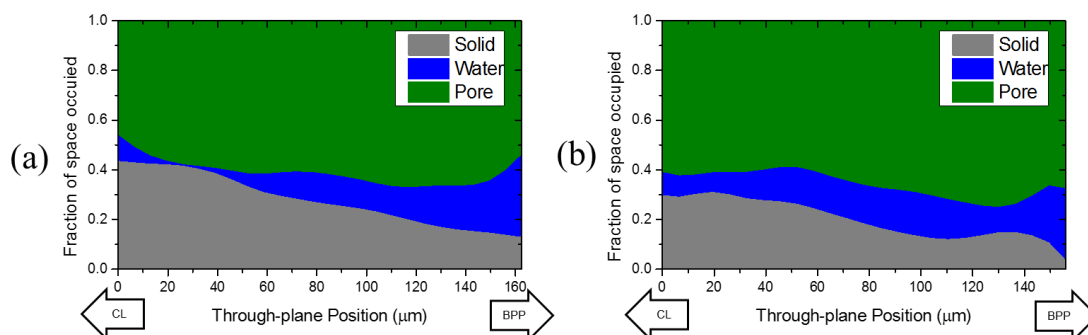

Figure 4. Effective porosity, liquid water and solid distributions in SGL 25 (a) BC and (b) BN, both at 2.5 A/cm^2

Conclusion

Two GDLs with and without MWCNTs in the MPL were studied to analyze the impact of a MWCNT-based MPL on the performance of the fuel cell. Better electrochemical performance was obtained with SGL 25 BN (with MWCNTs) than with 25 BC (without MWCNTs). Although a higher liquid water saturation was measured in an operating fuel cell with a MWCNT-based MPL than with a conventional MPL, a highly porous GDL induced by MWCNTs led to a higher effective porosity and improved overall oxygen transport.

Acknowledgments

References

1. S. Park, J. Lee and B. N. Popov, *Int. J. Hydrogen Energy,* **37,** 5850 (2012).
2. J. Morgan, and R. Datta, *J. Power Sources,* **251,** 269 (2014).
3. H. K. Atiyeh, K. Karan, B. Peppley, A. Phoenix, E. Halliop and J. Pharoah, *J. Power Sources,* **170,** 111 (2007).
4. Z. Qi and A. Kaufman, *J. Power Sources,* **109,** 38 (2002).
5. S. Park, J. Lee and B. N. Popov, *J. Power Sources,* **177,** 457 (2008).
6. U. Pasaogullari and C. Wang, *Electrochim. Acta,* **49,** 4359 (2004).
7. A. Z. Weber and J. Newman, *J. Electrochem. Soc.,* **152,** A677 (2005).
8. G. Park, Y. Sohn, S. Yim, T. Yang, Y. Yoon, W. Lee, K. Eguchi and C. Kim, *J. Power Sources,* **163,** 113 (2006).
9. H. Gharibi, M. Javaheri and R. A. Mirzaie, *Int. J. Hydrogen Energy,* **35,** 9241 (2010).
10. A. M. Kannan, A. Menghal and I. V. Barsukov, *Electrochemistry Communications,* **8,** 887 (2006).
11. A. M. Kannan and L. Munukutla, *J. Power Sources,* **167,** 330 (2007).
12. R. Schweiss, *Fuel Cells,* **16,** 100 (2016).
13. R. Schweiss, M. Steeb, P. M. Wilde and T. Schubert, *J. Power Sources,* **220,** 79 (2012).
14. S. Lin and M. Chang, *Int. J. Hydrogen Energy,* **40,** 7879 (2015).
15. G. Jung, W. Tzeng, T. Jao, Y. Liu and C. Yeh, *Appl. Energy,* **101,** 457 (2013).
16. T. Kitahara, H. Nakajima and K. Okamura, *J. Power Sources,* **283,** 115 (2015).
17. I. Manke, C. Hartnig, M. Grünerbel, W. Lehnert, N. Kardjilov, A. Haibel, A. Hilger, J. Banhart and H. Riesemeier, *Appl. Phys. Lett.,* **90,** 174105 (2007).
18. C. Hartnig, I. Manke, R. Kuhn, N. Kardjilov, J. Banhart and W. Lehnert, *Appl. Phys. Lett.,* **92,** 134106 (2008).
19. J. Haußmann, H. Markötter, R. Alink, A. Bauder, K. Dittmann, I. Manke and J. Scholta, *J. Power Sources,* **239,** 611 (2013).

20. H. Markötter, J. Haußmann, R. Alink, C. Tötzke, T. Arlt, M. Klages, H. Riesemeier, J. Scholta, D. Gerteisen, J. Banhart and I. Manke, *Electrochemistry Communications,* **34,** 22 (2013).

21. J. Lee, R. Yip, P. Antonacci, N. Ge, T. Kotaka, Y. Tabuchi and A. Bazylak, *J. Electrochem. Soc.,* **162,** F669 (2015).

22. I. V. Zenyuk, D. Y. Parkinson, G. Hwang and A. Z. Weber, *Electrochemistry Communications,* **53,** 24 (2015).

23. N. Ge, S. Chevalier, J. Hinebaugh, R. Yip, J. Lee, P. Antonacci, T. Kotaka, Y. Tabuchi and A. Bazylak, *J. of Synchrotron Radiation,* **23,** (2016).

24. P. Antonacci, S. Chevalier, J. Lee, N. Ge, J. Hinebaugh, R. Yip, Y. Tabuchi, T. Kotaka and A. Bazylak, *Electrochim. Acta,* **188,** 888 (2016).

25. J. Lee, R. Yip, P. Antonacci, N. Ge, T. Kotaka, Y. Tabuchi and A. Bazylak, *J. Electrochem. Soc.,* **162,** F669 (2015).

26. Z. Fishman and A. Bazylak, *J. Electrochem. Soc.,* **158,** B247 (2011).

27. Z. Fishman, J. Hinebaugh and A. Bazylak, *J. Electrochem. Soc.,* **157,** B1643 (2010).

28. S. Chevalier, J. Lee, N. Ge, R. Yip, P. Antonacci, Y. Tabuchi, T. Kotaka and A. Bazylak, *Electrochim. Acta,* **210,** 792 (2016).

29. R. Banerjee, J. Hinebaugh, H. Liu, R. Yip, N. Ge and A. Bazylak, *Int. J. Hydrogen Energy,* (2016).

30. M. George, Z. Fishman, S. Botelho and A. Bazylak, *J. Electrochem. Soc.,* **163,** F832 (2016).

31. Z. Fishman and A. Bazylak, *J. Electrochem. Soc.,* **158,** B247 (2011).

32. T. W. Wysokinski, D. Chapman, G. Adams, M. Renier, P. Suortti and W. Thomlinson, *Nuclear Instruments & Methods in Physics Research Section A-Accelerators Spectrometers Detectors and Associated Equipment,* **582,** 73 (2007).